Universal Kinetic Description for Thermal Decomposition of Copper(II) Hydroxide over Different Water Vapor Pressures

Masahiro Fukuda, Loïc Favergeon, Nobuyoshi Koga

Universal Kinetic Description for Thermal Decomposition of Copper(II) Hydroxide over Different Water Vapor Pressures

Masahiro Fukuda,† Loic Favergeon,‡ and Nobuyoshi Koga*,†

† Department of Science Education, Graduate School of Education, Hiroshima University, 1-1-1 Kagamiyama, Higashi-Hiroshima 739-8524, Japan

‡ Mines Saint-Etienne, University of Lyon, CNRS, UMR 5307 LGF, Centre SPIN, F-42023 Saint-Etienne, France

ABSTRACT: The impact that product gas in the reaction atmosphere has on the kinetics of the thermal decomposition of inorganic solids is an outstanding issue that requires a solution to understand the reactions in a solid−gas system. Among a variety of kinetic phenomena induced by atmospheric gas, the restraining effect of the overall reaction rate with increasing partial pressure of the product gas in the reaction atmosphere is the most widely observed phenomenon. In this study, we describe the universal kinetics of the thermal decomposition of solids over different temperatures and partial pressures of the gas, as exemplified by the thermal decomposition of $Cu(OH)_2$. Universal kinetic descriptions were enabled by introducing an accommodation function, with respect to atmospheric water vapor pressure, into the fundamental kinetic equation for solid-state reactions. The thermoanalytical curves as measured systematically under different temperatures and water vapor pressure conditions were kinetically analyzed in a step-by-step manner to attain kinetic modeling of the physico-geometrical consecutive process that comprises the induction period, surface reaction, and phase boundary-controlled reaction. The impact that atmospheric water vapor has on the kinetics of each physico-geometrical reaction step was separately evaluated using the universal kinetic approach.

1. INTRODUCTION

The thermal decomposition of solids, for example, A(s) ⇄ B(s) + C(g), is characterized by specific heterogeneous features attributed to the physico-geometrical events that occur during the reaction site formation via nucleation on the surface of reactant solid, A(s), and the advancement of an as-produced reaction interface recognized as a zone of locally enhanced reactivity.[1–4] Product gas C(g) removal by diffusion from the reacting site via the solid product B(s) surface layer and gas desorption from the reacting solid surface are also relevant physicochemical events that control the overall reaction rate. Crystal growth of B(s) in the as-produced surface product layer controls gaseous product diffusion path formation. The intensive parameters, including temperature and pressure, affect each component step of the physico-geometrical reaction differently, and the overall reaction rate varies in a complex reaction system. One such parameter that controls the overall kinetics of the thermal decomposition of solids is the partial pressure of the product gas, p(C(g)), in the reaction atmosphere, which has been extensively investigated since the early 20th century.[5]

Previous studies have reported a variety of kinetic phenomena induced by p(C(g)) effects, mainly for thermal dehydration and decarbonation reactions. The effects include deceleration interpreted as a normal effect with respect to chemical equilibrium for the reversible reaction,[6–16] acceleration via the catalytic effects,[17–25] opposite effects from two product gases on the overall rate,[21,23,26] and the

fluctuation of the overall reaction rate with p(C(g)) that appears as a combined effect of deceleration and acceleration, which is typically known as the Smith − Topley effect[27–29] that has been observed for the thermal dehydration of crystalline hydrates.[30]

The restraining effect that partial pressure of the product gas p(C(g)) has on the overall reaction rate of thermal decomposition, which is the most widely observed phenomenon,[6–16] has been subjected to rigorous kinetic description. The introduction of an accommodation function (AF) into the fundamental kinetic equation for solid-state reactions[3,31–35] is one possible way to formulate the kinetic equation that universally describes kinetic behavior at different temperature conditions and p(C(g)) values:

$$\frac{\mathrm{d}\alpha}{\mathrm{d}t} = A\exp\left(-\frac{E_\mathrm{a}}{RT}\right) f(\alpha) a\left(p\big(\mathrm{C(g)}\big), P_\mathrm{eq}(T)\right) \quad (1)$$

where α is the fractional reaction; A and E a are the apparent preexponential factor and activation energy, respectively; R is the gas constant; and f(α) is the kinetic model function derived by considering the physico-geometry of the reaction to describe changes in the overall reaction rate as the reaction advances. The AF, a(p(C(g)),P_{eq}(T)), is a function of p(C(g)) and the equilibrium pressure P_{eq}(T) of reversible thermal decomposition. Among the various functional forms of the AF proposed in previous studies,[6–8,36–46] the form expressed by eq 2 is the most widely used to account for the impact of p(C(g)) on the overall reaction rate:[6,7,42,46]

$$a\left(p\big(\mathrm{C(g)}\big), P_\mathrm{eq}(T)\right) = 1 - \frac{p\big(\mathrm{C(g)}\big)}{P_\mathrm{eq}(T)} \quad (2)$$

The AF in eq 2 corrects the overall reaction rate by considering the ratio of p(C(g)) with respect to P eq (T). The AF was originally derived by considering the contribution that the reverse reaction has to the overall reaction.6 Several studies have lately rederived this function by formulating different kinetic models, which include gas absorption on the intermediate layer,[9] gas diffusion through the surface product layer,[11] and active solid product formation.[46] The same function was also derived through the kinetic description of the overall reaction based on the transition state theory.[15] Possible distortions of E_a and its variation as a reaction advances were recently simulated on the basis of the kinetic equation (eq 1) with the AF in eq 2.[43,44]

A previous study has demonstrated the usefulness of the kinetic equation with the AF in eq 2 for the thermal decomposition of $CaCO_3$,[42] in which nearly identical values for E_a values were obtained for the reactions at different partial pressures of CO_2, p(CO_2), using the non-isothermal single run method by introducing eq 2. However, the study also found that Arrhenius-type plots for reactions at different p(CO_2) values shift systematically along reciprocal temperature coordinates with p(CO_2) values, which indicates the occurrence of individual linear correlations with different intercepts.[42] Therefore, the kinetic equation (eq 1), combined with the AF in eq 2, is not capable of universal kinetic description for reactions at different p(CO_2) values. The universal kinetic description that covers kinetic behavior at different p(C(g)) is strongly desired to obtain a more detailed understanding of kinetics in connection with the mechanistic features of heterogeneous reactions. Recently, we derived an alternative AF that enables the universal kinetic description of the thermal decomposition of metal hydroxides at different water vapor pressures, p(H_2O), through the theoretical consideration of elementary steps of nucleation and interfacial reaction, in which we

applied the rate-limiting step approximation; i.e., a selected elementary step regulates the overall reaction rate, while other elementary steps are at an equilibrium condition.[47]

$$a\left(p(\mathrm{H_2O}), P_{\mathrm{eq}}(T)\right) = \left[\frac{P_0}{p(\mathrm{H_2O})}\right]^a \left[1 - \left(\frac{p(\mathrm{H_2O})}{P_{\mathrm{eq}}(T)}\right)^b\right] \quad (3)$$

where P_0 is the standard pressure, which is introduced to express all pressure terms in the same unit. The product of two $p(H_2O)$ related parts expresses the analytical form of this AF, i.e., $[P_0/p(H_2O)]^a$ and $1-(p(H_2O)/P_{eq}(T))^b$. The exponents (a,b) in eq 3 describe the specific features of the impact that $p(H_2O)$ has on the reaction kinetics. When (a,b) = (0,1), eq 3 is equivalent to eq 2. When the second part of the AF, $1-(p(H_2O)/P_{eq}(T))^b$, is unity, the kinetic equation (eq 1) with the AF in eq 3 is formal kinetic equation that considers the $p(H_2O)$ as the inhibitor. The effectiveness of the kinetic equation (eq 1), together with the AF in eq 3, has been critically examined through stepwise kinetic analyses of thermal decomposition of $Ca(OH)_2$ using systematically measured mass-loss curves at different heating conditions when exposed to different, but controlled, $p(H_2O)$ values.[47]

The isothermal decomposition of $Ca(OH)_2$ in the presence of atmospheric water vapor was characterized by a significant induction period (IP) and subsequent sigmoidal mass-loss behavior. Increasing the $p(H_2O)$ systematically reduced the reaction rate in both the IP and mass-loss processes. A universal kinetic approach to reactions at different temperature profiles over different $p(H_2O)$ conditions was established through formal kinetic calculations using the Arrhenius- and Friedman-type plots applied to the IP and mass-loss process, respectively, in which the impact that $p(H_2O)$ has on the reaction rate was evaluated by the exponents, (a,b), in eq 3. Furthermore, reactions exposed to isothermal conditions were analyzed on the basis of the physico-geometrical consecutive model that comprises the IP, surface reaction (SR), and phase-boundary-controlled reaction (PBR). The impact that $p(H_2O)$ has on each physico-geometrical step was separately evaluated by applying the AF in eq 3 to the Arrhenius plot. The universal kinetic approach may yield further insights into reaction kinetics in solid−gas systems. This may be achieved by collecting the results of universal kinetic approaches for a series of reactions to classify correlation patterns among the kinetic parameters, including the exponents (a,b), and these variation trends as the reaction step advances.

We recently reported[48] that thermal decomposition of $Cu(OH)_2$ in flowing dry N_2 gas is kinetically characterized by the physico-geometrical consecutive process described in the IP−SR−PBR model, followed by the appearance of a reaction tail as trapped water molecules evolved with gradual crystal growth in the solid product, i.e., CuO. This reaction process allows us to study the impact that $p(H_2O)$ has on each reaction step in the consecutive IP−SR−PBR model. Since thermal decomposition of $Cu(OH)_2$ and basic copper(II) compounds are the most likely method to control CuO synthesis with the desired morphologies and microstructures,[17,18,20,26,49–56] we expect that an increased understanding of the effect that atmospheric $p(H_2O)$ has on reaction kinetics, in correlation with the physico-geometrical mechanisms, will provide important information for sophisticated material processing design. In this study, the thermal decomposition of $Cu(OH)_2$ was systematically traced under various temperature and $p(H_2O)$ conditions. The applicability of the universal kinetic approach to the current reaction was investigated in comparison with kinetic results obtained with the conventional kinetic calculations. The mutual relationships among the kinetic parameters determined for each reaction step via the universal kinetic approach, and these variation patterns as

the physico-geometrical step advanced, are discussed in connection with the impacts of atmospheric $p(H_2O)$ and the physico-geometrical reaction mechanisms. Then, the universal view of the kinetic features of thermal decomposition of $Cu(OH)_2$ over different temperature and $p(H_2O)$ conditions is summarized in comparison with previously obtained kinetic results for the thermal decomposition of $Ca(OH)_2$.[47]

2. EXPERIMENTAL SECTION

2.1. Sample Characteristics. The $Cu(OH)_2$ sample used in this study is the identical sample used in our previous study for the kinetic analysis of thermal decomposition exposed to a dry N_2 gas flow,[48] which was prepared by titrating an ammoniacal solution of $CuSO_4$ with a NaOH solution as described in detail in section S1 of the Supporting Information. In our previous study, we reported sample characterizations using powder X-ray diffractometry (XRD), Fourier-transform infrared spectroscopy (FT-IR), and simultaneous thermogravimetry (TG) − differential thermal analysis (DTA) measurement.[48] Morphological characteristics of sample particles have also been analyzed via microscopic observations using scanning electron microscopy (SEM), as well as with the Brunauer−Emmett−Teller (BET) single point method to determine a specific surface area. The sample was an agglomerate of needle-like crystals with a range in length of approximately 3−5 μm and a specific surface area of 5.28±0.03 $m^2\ g^{-1}$. The XRD pattern was in agreement with that previously reported for $Cu(OH)_2$ (orthorhombic, S.G.=C*mc*2_1(36), a=2.9471, b=10.5930, c=5.2564, ICDD-PDF 01-080-0656).[57,58] Only absorption peaks attributed to O−H stretching vibration and Cu−O−H bond were observed in the FT-IR spectrum. Upon sample heating in an inert gas atmosphere, the sample transformed to CuO via thermal decomposition: $Cu(OH)_2(s) \rightleftarrows CuO(s)+H_2O(g)$. The observed total mass loss, i.e., 18.67±0.19%, corresponds to that calculated according to the chemical equation above.

2.2. Kinetic Data Measurement at Different Water Vapor Pressures. TG − derivative TG (DTG) measurements for the sample in a flowing N_2-H_2O mixed gas, with various, but controlled, $p(H_2O)$ values, were performed using a TG − DTA Instruments (Thermoplus TG-8120, Rigaku) equipped with a humidity controller (HUM-1, Rigaku).[59] Approximately 3.00 mg samples were weighed into a platinum sample pan that is 5 mm in diameter and 2.5 mm in height. The weighed sample was placed in the TG−DTA Instruments and heated at a heating rate, β, of 5 K min^{-1} to a temperature between 323 and 343 K in flowing dry N_2 gas at a rate of 400 $cm^3\ min^{-1}$. Immediately after the sample temperature reached the predetermined temperature, the flowing gas was switched to an N_2-H_2O mixed gas with a controlled $p(H_2O)$ value between 0.14 and 15.5 kPa. The measurement system was stabilized for 30 min by holding the sample temperature at the temperature in the fl owing N_2-H_2O mixed gas at a rate of 400 $cm^3\ min^{-1}$. The sample was then further heated to 873 K at β = 5 K min^{-1} to record TG−DTG curves in the flowing N_2-H_2O mixed gas with controlled $p(H_2O)$ values.

By selecting three different $p(H_2O)$ values in the flowing N_2-H_2O mixed gas, i.e., approximately 0.14, 1.04, and 9.59 kPa, TG−DTG measurements for the sample (initial mass m_0 : approximately 3.00 mg) were performed under isothermal and linear non-isothermal conditions to collect a series of kinetic data at each $p(H_2O)$ value. After the measurement system was stable between a temperature range of 323 and 343 K in the flowing N_2-H_2O mixed gas with controlled $p(H_2O)$ values (flow rate: 400 $cm^3\ min^{-1}$), the sample was heated at β = 5 K min^{-1} to various predetermined temperatures. The sample

temperature was held at those temperatures to record a series of TG−DTG curves at different constant temperatures in the flowing N_2−H_2O mixed gas with controlled p(H_2O) values.

Similarly, a series of TG−DTG curves exposed to linear non-isothermal conditions were recorded by heating the sample to 873 K at different β values ($0.5 \leq \beta$ /K $min^{-1} \leq 5$). In several TG−DTG measurements under isothermal and linear non-isothermal conditions in flowing N_2-H_2O mixed gas, the measurement was stopped midway through the mass-loss process. The sample was then immediately cooled to room temperature in flowing dry N_2. The recovered sample was coated with a thin platinum layer by sputtering (JFC-1600, JEOL; 30 mA, 30 s), and the morphology of the partially decomposed sample was observed under an SEM (JSM-6510, JEOL).

3. RESULTS AND DISCUSSION

3.1. Impact of Atmospheric Water Vapor. Figure S1 in Supporting Information reports typical TG−DTG curves recorded in flowing N_2-H_2O mixed gas. The major mass-loss process occurred in a narrow temperature range that began at approximately 420 K, followed by a long reaction tail that continued to approximately 600 K. The comparable reaction behavior was observed for the same sample in flowing dry N_2 gas in our previous study.[48] The major mass-loss process covered more than 90% of the total mass-loss value. Crystal growth of the CuO product accompanied mass loss during the reaction tail, which suggests the evolution of trapped water in micropores and grain boundaries within poorly crystalline CuO.

Figure 1 reports the typical isothermal mass-loss behavior in flowing N_2-H_2O mixed gas characterized by different p(H_2O) values. After the sample attained the predetermined reaction temperature at time zero, an IP was clearly observed prior to the detection of mass loss (Figure 1a). The mass-loss curve corresponding to the major mass-loss process exhibited a sigmoidal shape, which indicates a maximum mass-loss rate midway through the mass-loss process. The total mass-loss value under isothermal conditions corresponded approximately to that of the major mass-loss process shown by the TG–DTG curves recorded under non-isothermal conditions. The overall mass-loss behavior under isothermal conditions is abstractly comparable with that reported for reactions performed in flowing dry N_2 gas.[48] Focusing on the mass-loss behavior at a selected temperature in flowing N_2-H_2O mixed gas characterized by different p(H_2O) values (Figure 1b,c), the larger retardation effect on both chemical processes appeared as IP and mass-loss processes were observed with increasing p(H_2O) values. The retardation effect that atmospheric water vapor has on the mass-loss process under non-isothermal conditions occurred with a systematic shift in the TG−DTG curves to higher temperatures with increasing p(H_2O), as shown in Figure 2. Detectable change in curve shape accompanied the shifts in TG−DTG curves (Figure 2a), which was quantitatively evaluated by monitoring the changes in the extrapolated onset temperature, T_{eo}, and peak temperature, T_p, and peak height at T_p in the DTG curve (Figure 2b). The temperature difference between T_{eo} and T_p initially decreased in the lower p(H_2O) region and subsequently increased with p(H_2O) values, which was compensated by accompanying changes in the peak height at T_p. The observed changes in the mass-loss behavior with p(H_2O) are different from our previous results for the thermal decomposition of $Ca(OH)_2$,[47] for which the non-isothermal mass-loss curves shifted to higher temperatures accompanied by a systematic increase in the DTG peak height with increasing p(H_2O).

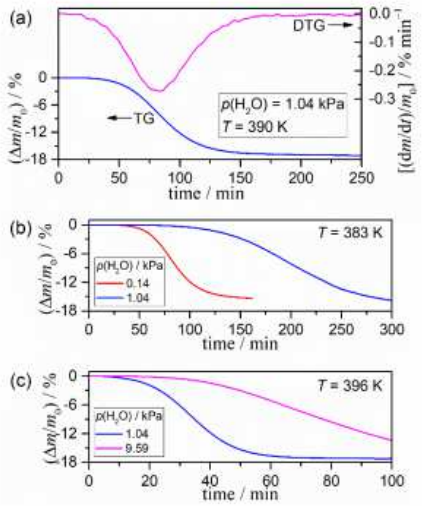

Figure 1. Specific features of isothermal mass-loss behavior of the thermal decomposition of $Cu(OH)_2$ in flowing N_2-H_2O mixed gas: (a) TG–DTG curves recorded at 390 K at $p(H_2O)$ = 1.04 kPa, (b) a comparison of TG curves recorded at 383 K under $p(H_2O)$ = 0.14 and 1.04 kPa, and (c) a comparison of TG curves recorded at 396 K under $p(H_2O)$ = 1.04 and 9.59 kPa.

A normal effect with respect to chemical equilibrium for the reversible reaction can explain the observed changes in the reaction behavior that depend on the $p(H_2O)$ value:

$$Cu(OH)_2(s) \rightleftarrows CuO(s) + H_2O(g) \quad (4)$$

Figure S2 shows the equilibrium water vapor pressure, $P_{eq}(T)$, at different temperatures, which was calculated using a thermodynamic database (MALT2, Kagaku Gijutsu-Sha),[60,61] together with the (T, $p(H_2O)$) region applied to the TG–DTG measurements to obtain the kinetic data. The atmospheric $p(H_2O)$ is lower than the $P_{eq}(T)$ during the course of the reaction. However, the relative intensity of $p(H_2O)$ with respect to $P_{eq}(T)$ varies with reaction temperature during isothermal measurements at a selected $p(H_2O)$ and with the applied $p(H_2O)$ during measurements at a selected reaction temperature. In the non-isothermal measurements, the $p(H_2O)/P_{eq}(T)$ ratio varies depending on $p(H_2O)$ and β , as well as reaction advancement. If the variation in the $p(H_2O)/P_{eq}(T)$ ratio is the major cause of systematic changes in the TG–DTG curves, this variation can either be explained by the second component in the AF of eq 3, $1-(p(H_2O)/P_{eq}(T))^b$, or the conventional AF in eq 2. If the $p(H_2O)/P_{eq}(T)$ ratio is small and the b value is large, the second component in the AF of eq 3 is approximated to be unity.

Then, the kinetic equation with the first component in the AF of eq 3, $[P_0/p(H_2O)]^a$, becomes similar to the homogeneous kinetic equation considering the effect of the inhibitor.

Figure S3 illustrates the morphological changes in the sample particles during thermal decomposition with the presence of atmospheric water vapor. No distinguishable change in particle dimension and surface texture was detected during the IP (Figure S3a). The original needle-like crystals were cleaved in the length direction and branched during the major mass-loss process under isothermal conditions (Figure S3b,c), and each branch constricted in an approximately regular interval at the end of the major mass-loss process (Figure S3d). These textural changes are nearly identical with those observed in flowing dry N_2 gas.[48] Distinguishable textural differences between

decomposed samples in flowing dry N_2 and N_2–H_2O mixed gas appeared during the reaction tail and for the final CuO product. In flowing N_2–H_2O mixed gas, the surfaces of the constricted needle-like crystals, which were produced at the end of the major mass-loss process, yielded smooth surfaces during the reaction tail (Figure S3e), and needle-like crystals changed to linearly concatenated spherical crystal bodies when heated to 873 K (Figure S3f). Textural changes in the reacting sample and solid product during the reaction tail indicate the enhancement of sintering and CuO crystal growth induced by atmospheric water vapor.

3.2. Kinetics of the Induction Period at Different Water Vapor Pressures. Figure 3 shows the isothermal mass-loss curves for the thermal decomposition of $Cu(OH)_2$ sample at different temperatures in flowing N_2-H_2O mixed gas with different $p(H_2O)$ values. To record a comparable series of isothermal mass-loss curves at different $p(H_2O)$ values, the measurement temperature range was slightly shifted to higher temperatures with increasing $p(H_2O)$ values. In each series of mass-loss curves at selected $p(H_2O)$ values, the duration of the IP, t_{IP}, was systematically prolonged with decreasing reaction temperatures. The t_{IP} value was obtained from the isothermal mass-loss curves based on an empirical definition, i.e., from the time at which the sample temperature attained the programmed constant temperature to the time at which the curve indicated a mass-loss value of 0.15% with respect to the initial sample mass, m_0. Figure 4 illustrates the changes in the t_{IP} value with temperature for the IP processes at different $p(H_2O)$ values. An exponential increase in t_{IP} value with decreasing temperature for the IP process under selected $p(H_2O)$ value is clearly observed, together with a systematic increase in t_{IP} values at a selected temperature with increasing $p(H_2O)$ values.

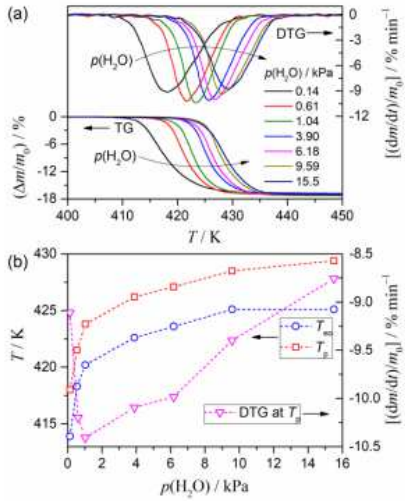

Figure 2. Changes in the mass-loss behavior under non-isothermal conditions depending on the $p(H_2O)$ value in the reaction atmosphere: (a) TG–DTG curves recorded at 5 K min^{-1} at different $p(H_2O)$ values and (b) changes in the extrapolated onset temperature (T_{eo}), peak temperature (T_p), and peak height at T_p in the DTG curves depending on the $p(H_2O)$ value.

The reciprocal of t_{IP} has been interpreted as the average reaction rate of the IP process. Therefore, eq 1 is applicable by assuming a zero-order process where $f(\alpha) = 1$.[62] Since the fractional conversion of the IP process, at which the conversion rate is equivalent to the averaged rate, t_{IP}^{-1}, can be constant for the IP process at different temperatures and $p(H_2O)$ values, eq 1 can be applied to an isoconversional plot in a differential form.[48,56,62 – 66] By taking the logarithms of eq 1 after substituting

the conversion rate from the reciprocal of t_{IP}, the Arrhenius-type plot for the IP process is examined based on the following equation:

$$\ln\left[\frac{1}{t_{\mathrm{IP}}\cdot a\left(p(\mathrm{H_2O}),P_{\mathrm{eq}}(T)\right)}\right] = \ln[A_{\mathrm{IP}}f(\alpha_{\mathrm{IP}})] - \frac{E_{\mathrm{a,IP}}}{RT} \quad (5)$$

where α_{IP}, A_{IP}, and $E_{a,IP}$ are the fractional conversion, preexponential factor, and apparent activation energy for the IP process, respectively. The fundamental kinetic equation that assumes $a(p(H_2O),P_{eq}(T)) = 1$ is applicable only to processes not influenced by atmospheric water vapor or for kinetic data recorded when exposed to negligible water vapor conditions.

Since t_{IP} variation depends on the $p(H_2O)$ value, as well as temperature, we are unable to obtain a universal kinetic description for the IP process by applying the fundamental kinetic equation. A trial application of the fundamental kinetic equation to the IP process at different temperatures and $p(H_2O)$ values resulted in individual Arrhenius-type plots for the processes at respective $p(H_2O)$ values, as is shown in Figure S4. The slope of the Arrhenius plot decreased with increasing $p(H_2O)$ values, which was accompanied by a compensatory decrease in the intercept. Variations in the conventional Arrhenius plot, when applied to the IP process, indicate trends that are completely opposite of those previously reported for the IP process during the thermal decomposition of $Ca(OH)_2$ at various $p(H_2O)$ values,[47] in spite of the similar retardation effect that $p(H_2O)$ has on the IP processes. Table S1 lists the apparent Arrhenius parameters determined for the IP processes of the thermal decomposition of $Cu(OH)_2$ at each $p(H_2O)$ value. The apparent Arrhenius parameters determined for the processes at different $p(H_2O)$ values indicate the compensatory variations between $E_{a,IP}$ and ln A_{IP}, otherwise known as the kinetic compensation effect (KCE),[67–74] i.e., the linear correlation observed between the experimentally determined E_a and ln A values. The decrease in the apparent A_{IP} value as atmospheric $p(H_2O)$ increases reasonably explains retardation of the IP process due to atmospheric $p(H_2O)$, but the decrease in the apparent $E_{a,IP}$ value is the opposite of the actual variation in kinetic behavior. Thus, the variation in the apparent Arrhenius parameters with $p(H_2O)$ values, determined by the conventional Arrhenius plot without considering the $p(H_2O)$ effect, can be interpreted as variations induced by effects from $p(H_2O)$ on the preexponential factor. Variations in apparent $E_{a,IP}$ values result as a consequence of the KCE. Therefore, the introduction of an appropriate AF, $a(p(H_2O),P_{eq}(T))$, is necessary to universally describe the kinetics of the IP process during the thermal decomposition of $Cu(OH)_2$ at various $p(H_2O)$ conditions. We can possibly aid primary examinations by introducing the AF from eq 2 into eq 5, which is widely used for the empirical kinetic analysis of thermal decomposition of solids at various partial pressures of the product gas. However, this examination was not necessarily successful and resulted in no dramatic improvements to the conventional Arrhenius-type plot that was empirically analyzed without considering $p(H_2O)$ effects. The modified Arrhenius-type plot that accompanied the AF in eq 2 also exhibited different linear correlations for the IP processes at different $p(H_2O)$ values, as shown in Figure S5. Table S1 also lists the apparent Arrhenius parameters determined from the modified Arrhenius plot for the IP processes at each $p(H_2O)$ value. The apparent Arrhenius parameters decreased with increasing $p(H_2O)$ values. Although the apparent Arrhenius parameters for the IP processes at $p(H_2O)$ values of 0.14 and 1.04 kPa were nearly identical with those determined by the conventional Arrhenius-type plot, we observed statistically significant decreases in both apparent Arrhenius parameters when compared with those determined using a conventional Arrhenius-type plot for the IP process at $p(H_2O)$ = 9.59 kPa. The difference in the variation of the apparent Arrhenius

parameters with respect to those determined by the conventional Arrhenius-type plot at each $p(H_2O)$ value is a different contribution of the AF in eq 2. The value in eq 2 is approximately unity for all data points at different temperatures in IP processes at $p(H_2O)$ values of 0.14 and 1.04 kPa. In contrast, the value changes from approximately 0.70 to 0.85 when increasing the temperature from 384 to 403 K for the IP process at $p(H_2O)$ = 9.59 kPa. Thus, the AF in eq 2 does not explain the change in the kinetics of the IP process with $p(H_2O)$ values below the lower $p(H_2O)$ region and does not enable universal kinetic descriptions at various $p(H_2O)$ conditions.

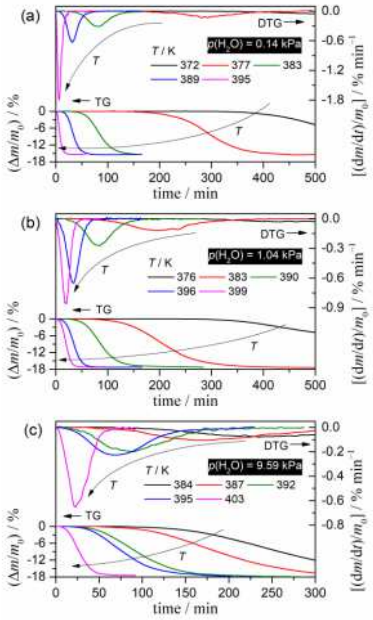

Figure 3. TG–DTG curves for the thermal decomposition of $Cu(OH)_2$ sample recorded at different constant temperatures under different $p(H_2O)$ values: (a) 0.14 kPa, (b) 1.04 kPa, and (c) 9.59 kPa.

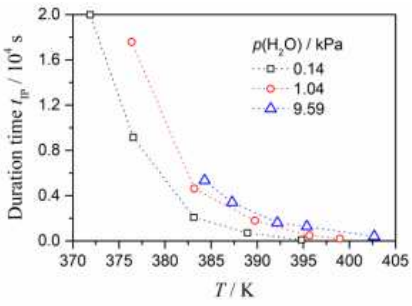

Figure 4. Change in t_{IP} value with temperature for the IP processes at different $p(H_2O)$ values.

When we introduce the AF in eq 3 into eq 5 as a novel kinetic approach to IP processes at various $p(H_2O)$ conditions, the exponents (a,b) in eq 3 should be determined by examining the modified Arrhenius-type plot. In practical kinetic analyses of IP processes at different $p(H_2O)$ values, the (a,b) values that yield the best linear correlations in the modified Arrhenius-type plot, including all data points at different temperature and $p(H_2O)$ conditions, were optimized using the Levenberg−Marquardt algorithm. Figure 5 shows the modified Arrhenius-type plot with the AF in eq 3. By setting exponents (a,b) to (0.42,12.85), a single Arrhenius-type plot can describe all data points of IP processes with a statistically significant correlation coefficient derived from linear regression

analysis (γ=−0.9830). The exponents, (0.42,12.85), explain the characteristics of the effect that $p(H_2O)$ has on the IP process. We normally do not expect such a large b value, i.e., 12.85, based on the theoretical examination of surface nucleation processes to derive the AF in eq 3.[47] In practice, the second component in eq 3, i.e., $1-(p(H_2O)/P_{eq}(T))^b$, approaches unity as the b value increases, which is due to $p(H_2O)/P_{eq}(T)<1$, as illustrated in Figure S2. Therefore, the first component in eq 3, i.e., $[P_0/p(H_2O)]^a$ where a=0.42, describes the effect that $p(H_2O)$ has on the kinetics of IP process,. The kinetic expression with $[P_0/p(H_2O)]^a$ as the AF in eq 1 is superficially identical to that for the chemical process influenced by the inhibitor. On the basis of the modified Arrhenius-type plot illustrated in Figure 5, the apparent Arrhenius parameters ($E_{a,IP}$ /kJ mol^{-1}, $\ln[A_{IP}f(\alpha_{IP})/s^{-1}]$) were determined to be (243.3±12.6, 66.1±3.9). The kinetic parameters, including the exponents (a,b) in the AF, universally describe the IP process of the thermal decomposition of $Cu(OH)_2$ at different temperatures under various $p(H_2O)$ values.

3.3. Kinetics of the Mass-Loss Process at Different Water Vapor Pressures. Figure 6 shows TG−DTG curves for the thermal decomposition of the $Cu(OH)_2$ sample recorded at different β and $p(H_2O)$ values, which were used for kinetic calculations of the mass-loss process, together with those recorded under isothermal conditions (Figure 3). The major mass-loss process before the distinguishable reaction tail was subjected to the kinetic study. TG−DTG curves recorded under isothermal and nonisothermal conditions were transferred to the kinetic curves that comprise data points (t, T, dα/dt, α) by defining the fractional reaction α with respect to the total mass-loss value during the major mass-loss process. Application of the differential isoconversional method, which evaluates the kinetic characteristics of the reaction by focusing on the dependence of the reaction rate on temperature at a selected α value, is one possible way to simultaneously analyze the mass-loss processes under isothermal and non-isothermal conditions. We derive eq 6 by taking the logarithms of eq 1.

$$\ln\left[\left(\frac{\mathrm{d}\alpha}{\mathrm{d}t}\right)\cdot\frac{1}{a\left(p(\mathrm{H_2O}),P_{\mathrm{eq}}(T)\right)}\right]=\ln[Af(\alpha)]-\frac{E_{\mathrm{a}}}{RT} \tag{6}$$

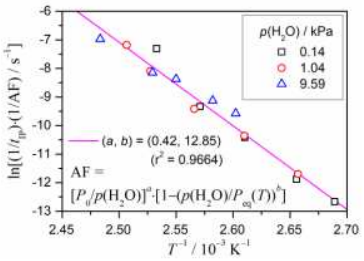

Figure 5. Universal Arrhenius-type plot based on eq 5 for the IP process of the thermal decomposition of $Cu(OH)_2$ over different $p(H_2O)$ values, obtained by introducing the AF in eq 3.

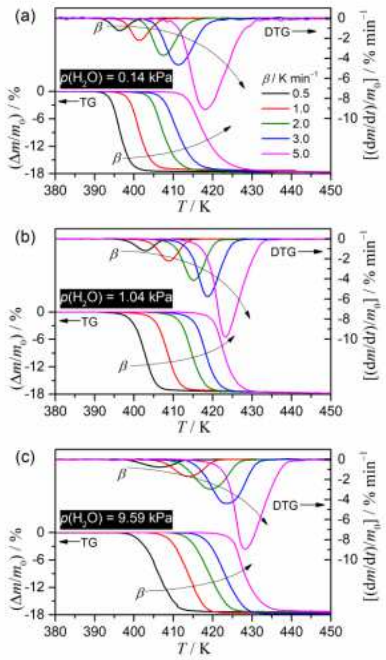

Figure 6. TG–DTG curves for the thermal decomposition of $Cu(OH)_2$ sample recorded at different β values under different $p(H_2O)$ values: (a) 0.14 kPa, (b) 1.04 kPa, and (c) 9.59 kPa.

If we assume that $a(p(H_2O),P_{eq}(T))$ is unity, as in conventional kinetic analysis, the plot of $\ln(d\alpha/dt)$ versus T^{-1} for the data points at a selected α, extracted from the series of kinetic curves, should yield a straight line with a slope of $-E_a/R$, which is the conventional Friedman plot.75 As a preliminary kinetic approach to the mass-loss process, the series of isothermal and non-isothermal kinetic curves for the mass-loss process at a given $p(H_2O)$ value was analyzed by applying the conventional Friedman plot without considering effects from $p(H_2O)$. Figure S6 reports the conventional Friedman plots at different α for the mass-loss processes at different $p(H_2O)$ values, and Figure 7 compares the results of the kinetic analysis among the processes at different $p(H_2O)$ values. The Friedman plots for each kinetic curve series at a given $p(H_2O)$ value exhibited statistically significant linear correlations with correlation coefficients, γ , better than −0.99, regardless of the value of α (Figure S6). The slope of the Friedman plots was approximately constant at different α.

These features in the Friedman plot were observed for all kinetic curve series at different $p(H_2O)$ values. By comparing the Friedman plots at a fixed α among the kinetic curve series at different $p(H_2O)$ values, we observe a parallel translation in the linear correlation to higher temperatures with increasing $p(H_2O)$ values without significant changes in the slope (Figure 7a). A decrease in the intercept of the plot accompanied this translation in the Friedman plot. The E_a values, at different α, calculated from the slope in the Friedman plots were approximately constant for each kinetic curve series recorded at a given $p(H_2O)$ value. In the α range from 0.20 to 0.80, the E_a values for reactions at different $p(H_2O)$ values nearly converged to values in an approximate range of 140−155 kJ mol^{-1}, which overlaps the range of standard deviation for each E_a value.

On the basis of the approximation that the mass-loss process at each $p(H_2O)$ condition is described by the constant E_a value during the course of a reaction, we reproduced the rate behaviors, which correspond to the change in reaction rate as the reaction advances, by projecting the reaction rate

at the real temperature to infinite temperature. At a given α, the hypothetical reaction rate, dα/dθ, at infinite temperature can be calculated according to the following equation.[76 – 80]

$$\left(\frac{d\alpha}{d\theta}\right) = \left(\frac{d\alpha}{dt}\right) exp\left(\frac{E_a}{RT}\right) = Af(\alpha) \qquad \text{with} \qquad \theta = \int_0^t exp\left(-\frac{E_a}{RT}\right) \tag{7}$$

where θ is Ozawa's generalized time,[81,82] which denotes the hypothetical reaction time at infinite temperature. The average E_a value in the α range from 0.2 to 0.8, calculated from the slope in the Friedman plots, was used to calculate the (dα/dθ) value at each α. According to eq 7, the relationship between (dα/dθ) and α can be used as an experimental master plot by correlating (dα/dθ) and f(α) with reduced values and normalizing those values with reference to the respective values at α = 0.5, i.e., $(d\alpha/d\theta)_{0.5}$ and f(0.5):[76–80]

$$\frac{(d\alpha/d\theta)}{(d\alpha/d\theta)_{0.5}} = \frac{f(\alpha)}{f(0.5)} \tag{8}$$

There is a close resemblance between the experimental master plots drawn for the mass-loss process at different $p(H_2O)$ conditions (Figure 7c), from which we expected a less significant influence of atmospheric $p(H_2O)$ on changes in reaction rate behavior as the reaction advances. The experimental master plots exhibit a maximum (dα/dθ) value midway through the reaction, as expected from the sigmoidal mass-loss curves recorded under isothermal conditions (Figures 1 and 3). Furthermore, the apparent A values were evaluated by fitting the experimental master plots, i.e., (dα/dθ) versus α, with an empirical kinetic model function, known as Sestak–Berggren model, SB(m, n, p):[31,83,84]

$$f(\alpha) = \alpha^m(1-\alpha)^n[-ln(1-\alpha)]^p \tag{9}$$

Table S2 lists the apparent kinetic parameters determined separately for the mass-loss processes at different $p(H_2O)$ conditions using a formal kinetic analysis based on the isoconversional kinetic relationship without considering $p(H_2O)$ effects. The results of the formal kinetic analysis without considering the influence of $p(H_2O)$ clearly indicate the necessity of an appropriate AF to obtain a universal kinetic description for the mass-loss process of the thermal decomposition of $Cu(OH)_2$ at different $p(H_2O)$ conditions, because the conventional Friedman plot for the reactions at different $p(H_2O)$ values indicates different linear correlations with different intercept (Figure 7a). However, the trial application of introducing the AF from eq 2 into eq 6 failed to yield the desired universal kinetic description. Instead, we obtained the individual linear correlations in the modified Friedman plot for the mass-loss processes at respective $p(H_2O)$ conditions, as shown in Figure S7. The results of the modified Friedman plot with the AF from eq 2 are nearly comparable with results from the conventional Friedman plot, although the introduction of the AF slightly improved linearity of the plots. Thus, we introduced the AF from eq 3 into eq 6 as a novel approach to attain universal kinetic description at any $p(H_2O)$ condition.

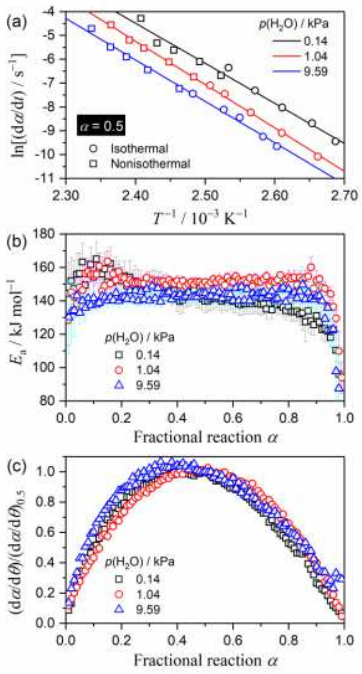

Figure 7. A comparison of the results of isoconversional kinetic analysis for the mass-loss process of the thermal decomposition of $Cu(OH)_2$ at different $p(H_2O)$ conditions: (a) Friedman plots at α = 0.5, (b) E_a values at different α, and (c) normalized experimental master plots of $(d\alpha/d\theta)/(d\alpha/d\theta)_{0.5}$ versus α.

Similar to the case where we applied the AF in eq 3 to the IP process, we optimized the exponents (a, b) in eq 3 to obtain the best linearity of the modified Friedman plot applied for all data points at various temperature and $p(H_2O)$ conditions. Figure 8 and Figure S8 report the results of the modified isoconversional kinetic analysis based on eq 6 with the AF from eq 3. By optimizing exponents (a, b) in eq 3, all data points at the selected α form a line, as shown in Figure 8a, which is generally observed for data points at a given α during the course of the reaction (Figure S8). In this kinetic calculation procedure, exponents (a,b) and these variation trends as the reaction advances are the important kinetic parameters that describe the impact of $p(H_2O)$. The approximately constant a value was optimized during the course of a reaction, characterized by a value of 0.36 ± 0.03 averaged over the range of $0.05 \leq \alpha \leq 0.95$ (Figure 8b). On the other hand, b values larger than 8.0 were determined during the course of a reaction. Since the $p(H_2O)$ values applied to the measurements were smaller than $P_{eq}(T)$, the second part of the AF in eq 3, i.e., $1-(p(H_2O)/P_{eq}(T))^b$, is approximated to be unity for all data points with such large b values. Therefore, the first part of the AF in eq 3, i.e., $[P_0/p(H_2O)]^a$ where a = 0.36±0.03, describes the impact that $p(H_2O)$ has on the kinetics of the mass-loss process of the thermal decomposition of $Cu(OH)_2$. As in the case of the IP process, the universal kinetic expression for the mass-loss process that consider the impact of $p(H_2O)$ resembles the chemical process with an inhibitor. The apparent E_a value evaluated using the modified Friedman plot with the AF in eq 3 indicated an approximately constant value over a wide α range with the average E_a value of 148.1±3.3 kJ mol^{-1} ($0.05 \leq \alpha \leq 0.90$).

3.4. Kinetic Descriptions Based on the Physico-Geometrical Consecutive Reaction Model. As previously mentioned, the kinetic equation (eq 1), which accounts for the impact of $p(H_2O)$ using the AF in eq 3, enables the universal kinetic description for the thermal decomposition of $Cu(OH)_2$ at various temperature and atmospheric $p(H_2O)$ conditions with respect to the Arrhenius- and Friedman-type plots. In additions to this, the objective is to correlate the universal kinetic approach

with the physico-geometric reaction mechanism, because the impact of $p(H_2O)$ possibly varies during different reaction stages in the thermal decomposition of solids. Previous studies have shown that the physico-geometric consecutive reaction model successfully illustrates the thermal decomposition of $Cu(OH)_2$, which comprises successive IP, SR, and PBR steps, followed by the gradual release of trapped water as the CuO crystal grows with further heating.[48] The typical feature of IP−SR−PBR model[64] is also observed for reactions performed under atmospheric water vapor as IP and subsequent sigmoidal mass-loss curves under isothermal conditions. The kinetic analysis of the consecutive surface and internal reactions originates from Mampel's kinetic equation in the case of isotropic growth of the nuclei[85] and, recently, reformalized as the nucleation and anisotropic growth model by Favergeon et al.[86] Ogasawara and Koga[64] derived the differential kinetic equations for this type of reaction under isothermal conditions, as the physico-geometrical consecutive IP−SR−PBR process. Table S3 in Supporting Information summarizes the differential kinetic equations derived by assuming a zero-order reaction for IP, first-order reaction for SR, and different dimensions, n (n=1−3), of the shrinkage of reaction interface for PBR. During practical kinetic calculation based on the IP−SR−PBR(n) model, the respective rate constants for IP, SR, and PBR(n) processes, k_{IP} ($=t_{IP}^{-1}$), k_{SR}, and $k_{PBR(n)}$, are optimized by nonlinear least-squares analysis.

In this study, the initial rate constant values for optimization were determined as follows. The initial k IP value was calculated from the apparent Arrhenius parameters determined with the conventional Arrhenius-type plots for the IP process at each $p(H_2O)$ value (Table S1). Similarly, the initial $k_{PBR(n)}$ value was calculated from the apparent kinetic parameters that were determined with the conventional isoconversional kinetic analysis for the mass-loss process at each $p(H_2O)$ value (Table S2). Then, the order of the k_{SR} value was determined by graphically comparing the fit of the calculated kinetic curve with the experimental kinetic curve. After setting the initial values, we ran parameter optimization to minimize the squares sum, F, of the difference between the experimental and calculated kinetic curves.

$$F = \sum_{i=1}^{N} \left[\left(\frac{\mathrm{d}\alpha}{\mathrm{d}t} \right)_{\mathrm{exp},i} - \left(\frac{\mathrm{d}\alpha}{\mathrm{d}t} \right)_{\mathrm{cal},i} \right]^2 \quad (10)$$

where N is the number of data points in a kinetic curve.

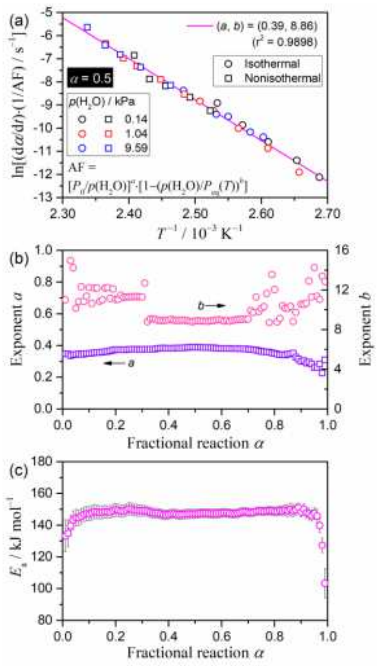

Figure 8. Results of the isoconversional kinetic analysis for the mass-loss process of the thermal decomposition of $Cu(OH)_2$ under different temperatures and $p(H_2O)$ conditions, modified by introducing the AF in eq 3: (a) the universal Friedman plot over different $p(H_2O)$ values at α=0.5, (b) the optimized exponents (a, b) in eq 3 at different α, and (c) E_a values at different α .

Figure 9 shows typical results for the curve fitting based on the IP−SR−PBR(n) model for the isothermal decomposition of $Cu(OH)_2$ at a given $p(H_2O)$ value. As was the case for thermal decomposition of the same sample in flowing N_2 gas,[48] the IP−SR−PBR(1) model was selected as the most appropriate kinetic model that exhibits a superior fit to the experimental kinetic curve compared with other models with n = 2 or 3. The optimized rate constants, i.e., k_{IP}, k_{SR}, and $k_{PBR(1)}$, for the kinetic data at different temperature and $p(H_2O)$ conditions are listed in Table S4, together with the determination coefficients used in the nonlinear least-squares analysis to fit the differential and integral kinetic curves.

Considering the impact that $p(H_2O)$ has on the reaction rate, eq 11 expresses the temperature dependence of k_{IP}, k_{SR}, and $k_{PBR(1)}$:

$$k = Aexp\left(-\frac{E_a}{RT}\right) a\left(p(H_2O), P_{eq}(T)\right) \tag{11}$$

By taking the logarithms of eq 11, we obtain eq 12:

$$\ln\left[\frac{k}{a\left(p(\mathrm{H_2O}),P_{\mathrm{eq}}(T)\right)}\right] = \ln\mathrm{A} - \frac{E_{\mathrm{a}}}{RT} \tag{12}$$

When we assume the AF, $a(p(H_2O),P_{eq}(T))$, is unity, without considering the impact of $p(H_2O)$, a plot of the left-hand side of eq 12 against T^{-1} is the conventional Arrhenius plot. Application of the conventional Arrhenius plot resulted in individual Arrhenius plots for each $p(H_2O)$ value in all physico-geometric reaction steps, as shown in Figure S9, which is easily expected on the basis of previously described results for processes at different $p(H_2O)$ values. Modi fi cations to the Arrhenius

plot by introducing the AF in eq 2 did not improve the results of individual Arrhenius plots, whereas we observed changes in the slope of the Arrhenius plot, especially for all physico-geometrical reaction steps at 9.59 kPa (see Figure S10). Table S5 lists the apparent Arrhenius parameters calculated from the modified Arrhenius plots with the AF in eq 2, as well as the conventional Arrhenius plots.

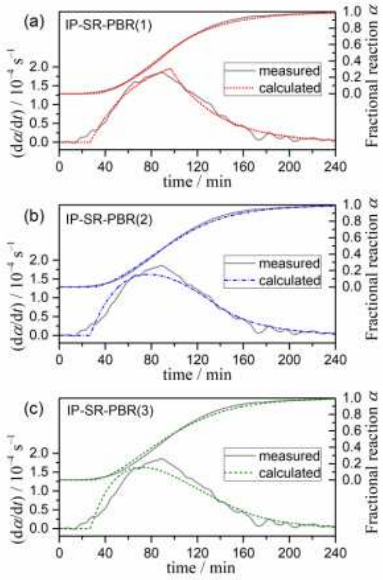

Figure 9. Typical results of the curve fitting based on the IP–SR–PBR(n) model for the isothermal decomposition of $Cu(OH)_2$ at 392 K under $p(H_2O)$ = 9.59 kPa: (a) n = 1, (b) n = 2, and (c) n = 3.

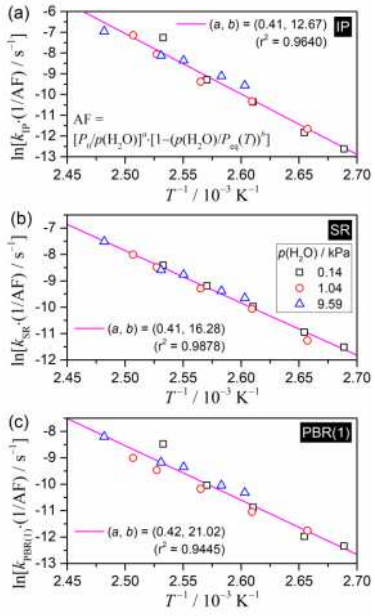

Figure 10. Universal Arrhenius plots for each physico-geometric reaction step in the thermal decomposition of $Cu(OH)_2$ over different $p(H_2O)$ conditions, enabled by introducing the AF in eq 3: (a) IP, (b) SR, and (c) PBR(1).

step	exponents		E_a / kJ mol^{-1}	ln(A / s^{-1})	$-\gamma^a$
	a	b			
IP	0.41	12.67	242.4 ± 13.0	65.8 ± 4.0	0.9819
SR	0.41	16.28	164.6 ± 5.1	41.6 ± 1.6	0.9939
PBR(1)	0.42	21.02	171.2 ± 11.5	42.9 ± 3.6	0.9718

[a] Correlation coefficient of the linear regression analysis.

Table 1. Optimized Exponents (a, b) in the AF of eq 3 and the Apparent Arrhenius Parameters for Each Reaction Step in the Thermal Decomposition of $Cu(OH)_2$ over different $p(H_2O)$ values

Figure 10 shows the Arrhenius plots for each physico-geometrical reaction step modified by introducing the AF in eq 3. Irrespective of the reaction step, single Arrhenius plot, accompanied by the exponents (a, b) in eq 3 optimized by plotting the left-hand side of eq 12 versus T−1 , universally illustrated the temperature dependence of the rate constant over di ff erent p(H 2 O) values. Table 1 lists the optimized exponents (a, b) and the apparent Arrhenius parameters calculated from the universal Arrhenius plots for each physico-geometric reaction step. The exponent a is approximately constant throughout the di ff erent reaction steps. The value a = 0.41 − 0.42 is comparable with those determined above using the modified Arrhenius plot for the IP process (Figure 5) and Friedman plot for the mass-loss process (Figure 8), combined with the AF in eq 3. The exponent b gradually increased with advancing the reaction step advances from IP to PBR via SR. However, values larger than 12 imply a less significant contribution from the second part of the AF, i.e., $1-(p(H_2O)/P_{eq}(T))^b$, to obtain the universal Arrhenius plot over different $p(H_2O)$ values. Therefore, for all physico-geometrical reaction steps, we can reduce the kinetic equation from eq 1 to eq 13:

$$\frac{d\alpha}{dt} = Aexp\left(-\frac{E_a}{RT}\right) f(\alpha) \left[\frac{P_0}{p(H_2O)}\right]^a \quad (13)$$

Equation 13 is the rate expression that considers the $p(H_2O)$ as the inhibitor, which indicates the completely different changes in the kinetic behavior depending on $p(H_2O)$ from those expected by the conventional understanding of the impact of evolved gas on the kinetic behavior based on the chemical equilibrium. Although the apparent Arrhenius parameters for IP, i.e., [E_a /kJ mol^{-1}, ln (A/s^{-1})]$_{IP}$, are nearly equivalent with those determined above, the values are larger, by approximately 20−25%, than those determined for IP in flowing dry N_2 gas in our previous study, (196.8±16.7, 54.3±5.1)$_{IP}$.[48] The apparent E_a values for the SR and PBR steps are larger than those determined for the mass-loss process using the modified Friedman plot with the AF in eq 3. The wider temperature region covered in the modified Friedman plot because of the kinetic data, which include data under isothermal and nonisothermal condition, is one reason for the difference, because the temperature interval is one of the parameters for the KCE.[69,70] The apparent Arrhenius parameters for SR and PBR(1) are also larger, by 25−30% and approximately 35%, respectively, than those determined for the respective reaction steps in flowing dry N_2 gas, (127.0±6.0, 32.9±1.8)$_{SR}$ and (124.6±6.0, 31.4±1.8)$_{PBR}$, respectively.[48] Superficially, the larger E_a values for the processes with the presence of water vapor explain the systematic shift in the kinetic curves to higher temperatures and the effect of $p(H_2O)$ as the inhibitor. However, the actual effect of atmospheric water vapor should be interpreted by considering the accompanying increase in A values in line with the KCE.[67–74] The kinetic parameters, including the exponents (a, b) for the IP, SR, and PBR(1) steps determined using eq 12 with the AF in eq 3, characterize the kinetic behavior of the thermal decomposition from different viewpoints, i.e., the dependence of the apparent reaction rate on conversion, temperature,

and $p(H_2O)$ in each physico-geometrical reaction step. The variations in each kinetic parameter as the consecutive reaction advances are also the kinetic characteristics of the reaction.

The exponents (a,b) and these variations as the reaction step advances are the specific kinetic characteristics obtained via the systematic measurement of the kinetic data under various temperatures and $p(H_2O)$ conditions and a universal kinetic approach to these kinetic data, which illustrates the impact of $p(H_2O)$ in connection with the physico-geometrical reaction step. A comparison of the kinetic characteristics with regard to the impact of $p(H_2O)$ or, more generally, the partial pressure of evolved gas in the reaction atmosphere with other reactions described by the IP−SR−PBR(n) model and classification of the kinetic characteristics are necessary tasks to provide further insight into the kinetic impact that atmospheric gas has on the thermal decomposition of inorganic solids. For example, although the impact of $p(H_2O)$ for all IP, SR, and PBR(1) steps during the thermal decomposition of $Cu(OH)_2$ was characterized by a constant exponent a (=0.41−0.42) and large exponent b (>12), we observed in our previous study the systematic decrease in exponent a from 4.75 to 3.36 as the reaction step advances, as well as an approximately constant b value (≈1.8) for all reaction steps for the thermal decomposition of $Ca(OH)_2$ at different $p(H_2O)$ conditions.

4. CONCLUSIONS

The thermal decomposition of $Cu(OH)_2$ with the presence of atmospheric water vapor exhibits a significant IP and sigmoidal mass-loss curve under isothermal conditions, which is nearly identical to the reaction in flowing dry N_2 gas observed in our previous study. Increasing $p(H_2O)$ in the reaction atmosphere suppresses reaction rates during IP and the mass-loss processes. The introduction of the AF with respect to $p(H_2O)$ and $P_{eq}(T)$ is necessary to universally describe kinetic behaviors of the reaction over different $p(H_2O)$. The AF in eq 3, formulated from the product of $[P_0/p(H_2O)]^a$ and $[1-(p(H_2O)/P_{eq}(T))^b]$, can be introduced to perform universal kinetic descriptions of both the IP and mass-loss processes through formal kinetic analysis using the Arrhenius- and Friedman-type plots, respectively. We optimized exponents (a,b) in eq 3 to yield the best universal linearity in the plots, which are important kinetic parameters to describe the kinetic characteristics of the reaction with respect to the impact of $p(H_2O)$. This is also applicable to the variations in the exponents (a,b) as the reaction advances for the results of the modified Friedman plot with the AF in eq 3. An evaluation of the exponents (a,b) for the IP and mass-loss processes exhibit comparable trends: exponent a was approximately 0.4, and the exponent b was larger than 8. The approximately constant a value during the course of the mass-loss process is also a specific character for the reaction. With the large b value, the second component of the AF, $1-(p(H_2O)/P_{eq}(T))^b$, is approximated to be unity; thus, the impact that $p(H_2O)$ has on the IP and mass-loss processes is described using the first component of the AF, $[P_0/p(H_2O)]^a$. Therefore, the kinetic equation that considers the AF superficially accounts for the effect of $p(H_2O)$ as the inhibitor. The apparent E_a values for the IP and mass-loss processes under various temperature and $p(H_2O)$ conditions were determined as 243.3±12.6 kJ mol^{-1} and 148.1±3.3 kJ mol^{-1}, respectively.

We were able to describe the thermal decomposition of $Cu(OH)_2$, which is characterized by IP and sigmoidal mass loss under isothermal conditions using the physico-geometrical consecutive process that comprises an IP with a zero-order process, SR with a first-order process, and PBR with a one-dimensional reaction interface movement, i.e., the IP−SR−PBR(1) model. The universal Arrhenius plots for the rate constants of each physico-geometrical reaction step, enabled by the modified

Arrhenius plot combined with the AF in eq 3, provide the exponents (a,b) for each physico-geometrical reaction step, as well as the apparent Arrhenius parameters.

Comparisons of these kinetic parameters, including the exponents (a, b), reveal the impact that $p(H_2O)$ has on reaction kinetics in connection with the physico-geometrical reaction mechanism. The exponents a, at approximately 0.4, and b, larger than 12, which are comparable with the results of the formal kinetic analysis based on the Arrhenius-type plot for IP and the Friedman plot for the mass-loss process, were invariant throughout the different physico-geometric reaction steps. The variation in the E_a value from 242.4±13.0 kJ mol^{-1} to 171.2±11.5 kJ mol^{-1}, as the physico-geometric reaction step proceeds from IP to PBR(1) via SR with 164.6±5.1 kJ mol^{-1}, is characteristic of the overall reaction, although we must account for the compensatory variation of the ln A value in line with the KCE when interpreting the variation in the E_a value.[67–74] The universal kinetic characterization over different temperatures and partial pressures of the gaseous product in the reaction atmosphere provides further insights into the kinetic and mechanistic understanding of the thermal decomposition of inorganic solids and the reactions in a solid − gas system. Comparisons of the results of the universal kinetic characterization among various thermal decomposition of solids may allow pattern classification for the relationships between the conventional kinetic triplet (E_a, A, f(α)) and exponents (a,b) in the AF, as well as variation trends in the kinetic parameters, including the exponents (a,b), as the reaction advances. Classification of the kinetic characteristics is a possible method to correlate apparent kinetic parameters with the mechanistic feature of the reaction.

■ AUTHOR INFORMATION

Corresponding Author

* Tel./fax: +81-82-424-7092. E-mail: nkoga@hiroshima-u.ac.jp.

ORCID

Loic Favergeon: 0000-0001-8181-867X

Nobuyoshi Koga: 0000-0002-1839-8163

Notes

The authors declare no competing financial interest.

■ ACKNOWLEDGMENTS

The present work was supported by JSPS KAKENHI Grant Numbers 17H00820.

■ REFERENCES

(1) Galwey, A. K.; Brown, M. E. Thermal Decomposition of Ionic Solids; Elsevier: Amsterdam, 1999.
(2) Galwey, A. K. Structure and Order in Thermal Dehydrations of Crystalline Solids. Thermochim. Acta 2000, 355, 181−238.
(3) Koga, N.; Tanaka, H. A Physico-Geometric Approach to the Kinetics of Solid-State Reactions as Exemplified by the Thermal Dehydration and Decomposition of Inorganic Solids. Thermochim. Acta 2002, 388, 41−61.

(4) Koga, N.; Goshi, Y.; Yoshikawa, M.; Tatsuoka, T. Physico-Geometrical Kinetics of Solid-State Reactions in an Undergraduate Thermal Analysis Laboratory. J. Chem. Educ. 2014, 91, 239−245.
(5) Spencer, W. D.; Topley, B. CCCLIV. − Chemical Kinetics of the System Ag2CO3 ⇄ Ag2O + CO2 . J. Chem. Soc. 1929, 0, 2633−2650.
(6) Benton, A. F.; Drake, L. C. Kinetics of Reaction and Adsorption in the System Silver−Oxygen. J. Am. Chem. Soc. 1934, 56, 255−263.
(7) Zawadzki, J.; Bretsznajder, S. Some Remarks on the Mechanism of Reactions of the Type: Solid = Solid + Gas. Trans. Faraday Soc. 1938, 34, 951−959.
(8) Hyatt, E. P.; Cutler, I. B.; Wadsworth, M. E. Calcium Carbonate Decomposition in Carbon Dioxide Atmosphere. J. Am. Ceram. Soc. 1958, 41, 70−74.
(9) Barret, P. Expression Theorique en Fonction de la Pression de la Loi de Vitesse de Croissance d'une Couche non Protectrice Formee par Decomposition Thermique d'un Solide. C. R. Acad. Sci. Paris, Ser. C 1968, 266, 856−859.
(10) Delmon, B. Introduction a la Cinetique Heterogene; Editions Technip: Paris, 1969.
(11) Searcy, A. W.; Beruto, D. Kinetics of Endothermic Decomposition Reactions. 2. Effects of the Solid and Gaseous Products. J. Phys. Chem. 1978, 82, 163−167.
(12) Barret, P. Cinetique Heterogene; Gauthier-Villars: Paris, 1973. (13) Bertrand, G.; Lallemant, M.; Watelle, G. Propos sur l'Interpretation de l'Energie d'Activation Experimentale. J. Therm. Anal. 1978, 13, 525−542.
(14) Maciejewski, M.; Badyga, J. The Influence of the Pressure of the Gaseous Product on the Reversible Thermal Decomposition of Solids. Thermochim. Acta 1985, 92, 105−108.
(15) Reading, M.; Dollimore, D.; Whitehead, R. The Measurement of Meaningful Kinetic Parameters for Solid State Decomposition Reactions. J. Therm. Anal. 1991, 37, 2165−2188.
(16) L'vov, B. V. Role of Vapour Oversaturation in the Thermal Decomposition of Solids. J. Therm. Anal. Calorim. 2009, 96, 321−330.
(17) Koga, N.; Criado, J. M.; Tanaka, H. Apparent Kinetic Behavior of the Thermal Decomposition of Synthetic Malachite. Thermochim. Acta 1999, 340 − 341, 387−394.
(18) Koga, N.; Criado, J. M.; Tanaka, H. Kinetic Analysis of the Thermal Decomposition of Synthetic Malachite by CRTA. J. Therm. Anal. Calorim. 2000, 60, 943−954.
(19) Koga, N. A Comparative Study of the Effects of Decomposition Rate Control and Mechanical Grinding on the Thermal Decomposition of Aluminum Hydroxide. J. Therm. Anal. Calorim. 2005, 81, 595−601.
(20) Koga, N.; Tatsuoka, T.; Tanaka, Y. Effect of Atmospheric water Vapor on the Kinetics of Thermal Decomposition of Copper(II) Carbonate Hydroxide. J. Therm. Anal. Calorim. 2009, 95, 483−487.
(21) Yamada, S.; Koga, N. Kinetics of the Thermal Decomposition of Sodium Hydrogen Carbonate Evaluated by Controlled Rate Evolved Gas Analysis Coupled with Thermogravimetry. Thermochim. Acta 2005, 431, 38−43.
(22) Koga, N.; Maruta, S.; Kimura, T.; Yamada, S. Phenomenological Kinetics of the Thermal Decomposition of Sodium Hydrogencarbonate. J. Phys. Chem. A 2011, 115, 14417−14429.
(23) Yamada, S.; Tsukumo, E.; Koga, N. Influences of Evolved Gases on the Thermal Decomposition of Zinc Carbonate Hydroxide Evaluated by Controlled Rate Evolved Gas Analysis Coupled with TG. J. Therm. Anal. Calorim. 2009, 95, 489−493.
(24) Koga, N.; Tatsuoka, T.; Tanaka, Y.; Yamada, S. Catalytic Action of Atmospheric Water Vapor on the Thermal Decomposition of Synthetic Hydrozincite. Trans. Mater. Res. Soc. Jpn. 2009, 34, 343−346.
(25) Nakano, M.; Fujiwara, T.; Koga, N. Thermal Decomposition of Silver Acetate: Physico-Geometrical Kinetic Features and Formation of Silver Nanoparticles. J. Phys. Chem. C 2016, 120, 8841−8854.

(26) Koga, N.; Yamada, S. Influences of Product Gases on the Kinetics of Thermal Decomposition of Synthetic Malachite Evaluated by Controlled Rate Evolved Gas Analysis Coupled with Thermogravimetry. Int. J. Chem. Kinet. 2005, 37, 346−354.
(27) Topley, B.; Smith, M. L. Function of Water Vapour in theDissociation of a Salt Hydrate. Nature 1931, 128, 302−302.
(28) Topley, B.; Smith, M. L. 69. Kinetics of Salt-Hydrate Dissociations: $MnC_2O_4{\cdot}2H_2O=MnC_2O_4+2H_2O$. J. Chem. Soc. 1935, 321−324.
(29) Volmer, M.; Seydel, G. Uber die Entwasserungsgeschwindigkeit des Manganooxalat-Dihydrats. Z. Phys. Chem. 1937, 179A, 153−171.
(30) L'Vov, B. V.; Novichikhin, A. V.; Dyakov, A. O. Computer Simulation of the Topley−Smith Effect. Thermochim. Acta 1998, 315, 169−179.
(31) Sestak, J. Diagnostic Limits of Phenomenological Kinetic Models Introducing the Accommodation Function. J. Therm. Anal. 1990, 36, 1997−2007.
(32) Koga, N. Physico-Geometric Kinetics of Solid-State Reactions by Thermal Analyses. J. Therm. Anal. 1997, 49, 45−56.
(33) Koga, N. Ozawa's Kinetic Method for Analyzing Thermoanalytical Curves. J. Therm. Anal. Calorim. 2013, 113, 1527−1541.
(34) Koga, N.; Sestak, J.; Simon, P., Some Fundamental and Historical Aspects of Phenomenological Kinetics in the Solid State Studied by Thermal Analysis. In Thermal Analysis of Micro, Nano- and Non-Crystalline Materials, Sestak, J.; Simon, P., Eds. Springer: Dordrecht, 2013; pp 1−28.
(35) Koga, N., Physico-Geometric Approach to the Kinetics of Overlapping Solid-State Reactions. In Handbook of Thermal Analysis and Calorimetry, 2nd ed.; Vyazovkin, S.; Koga, N.; Schick, C., Eds. Elsevier: Amsterdam, 2018; Vol. 6, pp 213−251.
(36) Clayton, C. K.; Whitty, K. J. Measurement and Modeling of Decomposition Kinetics for Copper Oxide-Based Chemical Looping with Oxygen Uncoupling. Appl. Energy 2014, 116, 416−423.
(37) Khinast, J.; Krammer, G. F.; Brunner, C.; Staudinger, G. Decomposition of Limestone: The Influence of CO_2 and Particle Size on the Reaction Rate. Chem. Eng. Sci. 1996, 51, 623−634.
(38) Yin, J.; Kang, X.; Qin, C.; Feng, B.; Veeraragavan, A.; Saulov, D. Modeling of $CaCO_3$ Decomposition under CO_2/H_2O Atmosphere in Calcium Looping Processes. Fuel Process. Technol. 2014, 125, 125−138.
(39) Criado, J. M.; Gonzalez, F.; Gonzalez, M. Influence of the CO_2 Pressure on the Kinetics of Thermal Decomposition of Manganese Carbonate. J. Therm. Anal. 1982, 24, 59−65.
(40) Criado, J. M.; Gonzalez, M.; Macias, M. Influence of CO_2 Pressure on the Kinetics of Thermal Decomposition of $CdCO_3$. Thermochim. Acta 1987, 113, 31−38.
(41) Criado, J. M.; Gonzalez, M.; Macías, M. Influence of CO_2 Pressure on the Kinetics of Thermal Decomposition of $PbCO_3$. Thermochim. Acta 1987, 113, 39−47.
(42) Criado, J.; Gonzalez, M.; Malek, J.; Ortega, A. The Effect of the CO_2 Pressure on the Thermal Decomposition Kinetics of Calcium Carbonate. Thermochim. Acta 1995, 254, 121−127.
(43) Liavitskaya, T.; Vyazovkin, S. Discovering the Kinetics of Thermal Decomposition during Continuous Cooling. Phys. Chem. Chem. Phys. 2016, 18, 32021−32030.
(44) Liavitskaya, T.; Vyazovkin, S. Delving into the Kinetics of Reversible Thermal Decomposition of Solids Measured on Heating and Cooling. J. Phys. Chem. C 2017, 121, 15392−15401.
(45) Deutsch, M.; Birkelbach, F.; Knoll, C.; Harasek, M.; Werner, A.; Winter, F. An Extension of the NPK Method to Include the Pressure Dependency of Solid State Reactions. Thermochim. Acta 2017, 654, 168−178.
(46) Ingraham, T. R.; Marier, P. Kinetic Studies on the Thermal Decomposition of Calcium Carbonate. Can. J. Chem. Eng. 1963, 41, 170−173.
(47) Koga, N.; Favergeon, L.; Kodani, S. Impact of Atmospheric Water Vapor on the Thermal Decomposition of Calcium Hydroxide: A Universal Kinetic Approach to a Physico-Geometric Consecutive Reaction in Solid − Gas System under Different Partial Pressures of Gas. Phys. Chem. Chem. Phys. 2019, 21, 11615−11632.

(48) Fukuda, M.; Koga, N. Kinetics and Mechanisms of the Thermal Decomposition of Copper(II) Hydroxide: A Consecutive Process Comprising Induction Period, Surface Reaction, and Phase Boundary-Controlled Reaction. J. Phys. Chem. C 2018, 122, 12869−12879.
(49) Tanaka, H.; Koga, N. Preparation and Thermal Decomposition of Basic Copper(II) Sulfates. Thermochim. Acta 1988, 133, 221−226.
(50) Tanaka, H.; Koga, N. The Thermal Decomposition of Basic Copper(II) Sulfate: An Undergraduate Thermal Analysis Experiment. J. Chem. Educ. 1990, 67, 612−614.
(51) Tanaka, H.; Kawano, M.; Koga, N. Thermogravimetry of Basic Copper(II) Sulphates Obtained by Titrating NaOH solution with $CuSO_4$ solution. Thermochim. Acta 1991, 182, 281−292.
(52) Koga, N.; Tanaka, H. Thermal Decomposition of Copper(II) and Zinc Carbonate Hydroxides by Means of TG − MS. J. Therm. Anal. Calorim. 2005, 82, 725−729.
(53) Tanaka, H.; Sadamoto, T. The Simultaneous Determination of the Kinetics and Thermodynamics of $Cu(OH)_2$ Decomposition by Means of TG and DSC. Thermochim. Acta 1982, 54, 273−280.
(54) Koga, N.; Criado, J. M.; Tanaka, H. Reaction Pathway and Kinetics of the Thermal Decomposition of Synthetic Brochantite. J. Therm. Anal. 1997, 49, 1467−1475.
(55) Frost, R. L.; Ding, Z.; Kloprogge, J. T.; Martens, W. N. Thermal Stability of Azurite and Malachite in Relation to the Formation of Mediaeval Glass and Glazes. Thermochim. Acta 2002, 390, 133−144.
(56) Koga, N.; Kimizu, T. Thermal Decomposition of Indium(III) Hydroxide Prepared by the Microwave-Assisted Hydrothermal Method. J. Am. Ceram. Soc. 2008, 91, 4052−4058.
(57) Oswald, H. R.; Reller, A.; Schmalle, H. W.; Dubler, E. Structure of Copper(II) Hydroxide, Cu(OH)2. Acta Crystallogr., Sect. C: Cryst. Struct. Commun. 1990, 46, 2279−2284.
(58) Cudennec, Y.; Lecerf, A. The Transformation of $Cu(OH)_2$ into CuO, Revisited. Solid State Sci. 2003, 5, 1471−1474.
(59) Arii, T.; Kishi, A. The Effect of Humidity on Thermal Process of Zinc Acetate. Thermochim. Acta 2003, 400, 175−185.
(60) Yokokawa, H.; Yamauchi, S.; Matsumoto, T. The Thermodynamic Database MALT. CALPHAD: Comput. Coupling Phase Diagrams Thermochem. 1999, 23, 357−364.
(61) Yokokawa, H.; Yamauchi, S.; Matsumoto, T. Thermodynamic Database MALT for Windows with gem and CHD. CALPHAD: Comput. Coupling Phase Diagrams Thermochem. 2002, 26, 155−166.
(62) Hansen, L. D.; Eatough, D. J.; Lewis, E. A.; Bergstrom, R. G.; Degraft-Johnson, D.; Cassidy-Thompson, K. Shelf-Life Prediction from Induction Period Calorimetric Measurements on Materials Undergoing Autocatalytic Decomposition. Can. J. Chem. 1990, 68, 2111−2114.
(63) Kimura, T.; Koga, N. Thermal Dehydration of Monohydrocalcite: Overall Kinetics and Physico-Geometrical Mechanisms. J. Phys. Chem. A 2011, 115, 10491−10501.
(64) Ogasawara, H.; Koga, N. Kinetic Modeling for Thermal Dehydration of Ferrous Oxalate Dihydrate Polymorphs: A Combined Model for Induction Period − Surface Reaction − Phase Boundary Reaction. J. Phys. Chem. A 2014, 118, 2401−2412.
(65) Simon, P. Induction Periods. J. Therm. Anal. Calorim. 2006, 84, 263−270.
(66) Kitabayashi, S.; Nakano, M.; Nishikawa, K.; Koga, N. Model Experiment of Thermal Runaway Reactions Using the Aluminum−Hydrochloric Acid Reaction. J. Chem. Educ. 2016, 93, 1261−1266.
(67) Koga, N.; Tanaka, H. A Kinetic Compensation Effect Established for the Thermal-Decomposition of a Solid. J. Therm. Anal. 1991, 37, 347−363.
(68) Koga, N.; Sestak, J. Kinetic Compensation Effect as a Mathematical Consequence of the Exponential Rate Constant. Thermochim. Acta 1991, 182, 201−208.
(69) Koga, N.; Sestak, J. Further Aspects of the Kinetic Compensation Effect. J. Therm. Anal. 1991, 37, 1103−1108.
(70) Koga, N. A Review of the Mutual Dependence of Arrhenius Parameters Evaluated by the Thermoanalytical Study of Solid-State Reactions: The Kinetic Compensation Effect. Thermochim. Acta 1994, 244, 1−20.

(71) Galwey, A. K.; Mortimer, M. Compensation Effects and Compensation Defects in Kinetic and Mechanistic Interpretations of Heterogeneous Chemical Reactions. Int. J. Chem. Kinet. 2006, 38, 464−473.
(72) Barrie, P. J. The Mathematical Origins of the Kinetic Compensation Effect: 1. The Effect of Random Experimental Errors. Phys. Chem. Chem. Phys. 2012, 14, 318−326.
(73) Barrie, P. J. The Mathematical Origins of the Kinetic Compensation Effect: 2. The Effect of Systematic Errors. Phys. Chem. Chem. Phys. 2012, 14, 327−336.
(74) Xu, D.; Chai, M.; Dong, Z.; Rahman, M. M.; Yu, X.; Cai, J. Kinetic Compensation Effect in Logistic Distributed Activation Energy Model for Lignocellulosic Biomass Pyrolysis. Bioresour. Technol. 2018, 265, 139−145.
(75) Friedman, H. L. Kinetics of Thermal Degradation of Cha-Forming Plastics from Thermogravimetry, Application to a Phenolic Plastic. J. Polym. Sci., Part C: Polym. Symp. 1964, 6, 183−195.
(76) Ozawa, T. Applicability of Friedman Plot. J. Therm. Anal. 1986, 31, 547−551.
(77) Koga, N. Kinetic Analysis of Thermoanalytical Data by Extrapolating to Infinite Temperature. Thermochim. Acta 1995, 258, 145−159.
(78) Gotor, F. J.; Criado, J. M.; Malek, J.; Koga, N. Kinetic Analysis of Solid-State Reactions: The Universality of Master Plots for Analyzing Isothermal and Nonisothermal Experiments. J. Phys. Chem. A 2000, 104, 10777−10782.
(79) Criado, J. M.; Perez-Maqueda, L. A.; Gotor, F. J.; Malek, J.; Koga, N. A Unified Theory for the Kinetic Analysis of Solid State Reactions under any Thermal Pathway. J. Therm. Anal. Calorim. 2003, 72, 901−906.
(80) Malek, J. The Kinetic Analysis of Non-Isothermal Data. Thermochim. Acta 1992, 200, 257−269.
(81) Ozawa, T. A New Method of Analyzing Thermogravimetric Data. Bull. Chem. Soc. Jpn. 1965, 38, 1881−1886.
(82) Ozawa, T. Non-Isothermal Kinetics and Generalized Time. Thermochim. Acta 1986, 100, 109−118.
(83) Sestak, J.; Berggren, G. Study of the Kinetics of the Mechanism of Solid-State Reactions At Increasing Temperatures. Thermochim. Acta 1971, 3, 1−12.
(84) Sestak, J. Rationale and Fallacy of Thermoanalytical Kinetic Patterns. J. Therm. Anal. Calorim. 2012, 110, 5−16.
(85) Mampel, K. L. Time Conversion Formulas for Heterogeneous Reactions at the Phase Boundaries of Solid Bodies, I: The Development of the Mathematical Method and the Derivation of Area Conversion Formulas. Z. Phys. Chem., Abt. A 1940, 187, 43−57.
(86) Favergeon, L.; Pijolat, M.; Soustelle, M. Surface Nucleation and Anisotropic Growth Models for Solid-State Reactions. Thermochim. Acta 2017, 654, 18−27.